Advanced Functional Materials

ADVANCED FUNCTIONAL MATERIALS
www.afm-journal.de

RESEARCH ARTICLE

Natural Microgels Overcome Nanoparticle Retention Barriers for Hyperthermia and Tumor Regression

Yu-Chien Lin[1,2] | Dongping Jiang[1] | Young Hwan Choe[1] | Chun-Yen Wu[3] | Yanzhang Xu[1] | Jingyu Deng[1] | Yawen Song[1,2] | Zeyan Zhuang[2] | Ren-Jei Chung[3] | Nam-Joon Cho[1,2,4]

[1]School of Materials Science and Engineering, Nanyang Technological University, Singapore, Singapore | [2]Singapore-HUJ Alliance for Research and Enterprise, Singapore HUJ Alliance Research Enterprise (SHARE), Singapore, Singapore | [3]Department of Chemical Engineering and Biotechnology, National Taipei University of Technology, Taipei, Taiwan | [4]Centre for Cross Economy Global, Nanyang Technological University, Singapore, Singapore

Correspondence: Ren-Jei Chung (rjchung@mail.ntut.edu.tw) | Nam-Joon Cho (njcho@ntu.edu.sg)

Received: 12 November 2025 | **Revised:** 7 December 2025 | **Accepted:** 19 December 2025

Keywords: cancer treatment | Fe_3O_4 | hyperthermia | liposome | pollen | sustainable materials | tumor regression

ABSTRACT

Clinical translation of nanoparticle (NP) based hyperthermia has long been constrained by poor tumor retention and rapid systemic clearance, resulting in transient and subtherapeutic heating. Here, we present a biodegradable, bioinspired carrier system derived from sunflower pollen microgels (PMs) that overcomes these limitations through geometry-guided retention and tumor-microenvironment-responsive degradation. The spiky exine architecture of PMs, mimicking the adhesive morphology of natural pollen, enables mechanical interlocking within tumor tissue, while cationic liposome coating facilitates electrostatic assembly of Fe_3O_4 NPs. The resulting PM/Lipo/NP composites achieve stable, homogeneous heating at therapeutic temperatures (44.9°C ± 0.3°C) under alternating magnetic fields for up to 21 days far exceeding the performance of free Fe_3O_4 NPs (39.6°C ± 0.4°C). In vivo, this prolonged retention drives near-complete tumor regression with no detectable systemic toxicity, and the pollen matrix gradually degrades under tumor-relevant oxidative conditions (H_2O_2, pH 6.5). This study presents a structure-driven delivery concept, showing that bioinspired microgels can function as biodegradable, shape-anchored platforms for sustained magnetic hyperthermia and effective local cancer therapy.

1 | Introduction

Despite decades of therapeutic innovation, cancer remains a leading cause of death worldwide, highlighting the need for localized, effective, and minimally invasive treatment modalities [1]. Magnetic hyperthermia, which utilizes superparamagnetic nanoparticles (NPs) to generate heat under an alternating magnetic field (AMF), holds great potential for selective tumor ablation [2]. However, clinical translation of NP-based magnetic hyperthermia remains limited, primarily due to poor tumor retention in vivo [3]. This limitation directly compromises localized heat generation, spatial precision, and overall therapeutic efficacy [4]. A major factor is the heavy reliance on the enhanced permeability and retention (EPR) effect [5]. Although widely accepted in preclinical studies, the EPR effect is inconsistent in human tumors due to heterogeneous vasculature, elevated interstitial pressures, and immune-mediated clearance [6]. Consequently, less than 1% of injected NPs typically reach tumors within 24 h [7–9]. This low EPR efficiency, combined with the failure of NP-based materials in physical therapies like magnetic hyperthermia to gain clinical approval, emphasizes the need for new delivery strategies that can bridge the gap between preclinical promise and clinical success.

To overcome EPR limitation, active transport and retention (ATR) strategies have been developed to improve NP tumor

accumulation and prolong intratumoral presence [10]. Three principal approaches have emerged to improve NP persistence: (i) size optimization, where larger particles (e.g., 398 nm PLGA, 500–800 nm silica) can extend retention up to ~4 days, compared to <2 days for 15 nm gold NPs [10–12]; (ii) surface modifications (e.g., PEGylation or hydrogel coatings) to reduce immune clearance [13, 14]; and (iii) tumor microenvironment (TME)-responsive coatings leveraging acidic pH or enzymatic activity to induce in situ NP aggregation or transformation, thereby enhancing local accumulation [15–17]. Among these, cationic liposome-coated NPs have shown promise by promoting transcytosis and enhancing uptake, achieving up to 10% tumor accumulation in preclinical models [10]. However, such increased uptake often accelerates immune recognition and systemic clearance, limiting long-term retention [18]. While these approaches improve initial delivery, sustaining NP presence within tumors remains a major challenge. Despite advances such as dual-responsive systems (e.g., pH/enzyme) [19], PEGylated and biodegradable formulations still exhibit >50% degradation or systemic clearance within 6–7 days [20]. However, retention durations of less than one week remain common, ultimately limiting the sustained thermal performance necessary for effective magnetic hyperthermia.

Another critical consideration is the precise thermal performance of retained NPs. Solid tumors have impaired heat dissipation, making them vulnerable to mild hyperthermia (42°C–46°C) [21]. Sustained temperatures in this range induce proteotoxic stress and reactive oxygen species (ROS) generation, which synergize with immune activation mechanisms such as enhanced antigen presentation and T cell cytotoxicity [22, 23]. Temperatures exceeding 46°C drive irreversible necrosis [24]. However, if NP retention is unstable, heating is transient and off-target effects may arise. Thus, long-term therapeutic efficacy in magnetic hyperthermia depends critically on both tumor-retained NPs and consistent, localized thermal delivery [22]. Thus, overcoming the intrinsic retention barrier remains major obstracle to translating NP-based hyperthermia from preclinical concept into clinical practice. Achieving durable and safe therapeutic heating in vivo will require a new design paradigm, one that seamlessly integrates sustained physical anchorage, tumor-responsive adaptability, and controlled biodegradability.

In this context, naturally derived PM have recently gained attention as structurally defined, mechanically robust, and biocompatible carriers capable of encapsulating therapeutic agents with high stability [25]. Sunflower-pollen–derived microgels, in particular, possess a uniform architecture, tunable permeability, and environmental responsiveness, offering inherent advantages for localized delivery and prolonged residence compared with synthetic polymeric systems [26]. These features suggest that PM may serve not only as passive carriers, but as structurally active scaffolds capable of enhancing intratumoral retention. Here, we introduce a bioinspired NP delivery system based on sunflower pollen microgels (PMs) that overcomes tumor retention and biodegradation challenges through geometry-guided retention and TME-responsiveness degradation (Scheme). The spiny exine of sunflower pollen, naturally evolved for adhesion during pollination, serves as a structural template for mechanical interlocking and prolonged surface anchorage [27]. Similar pollen-based microcapsule systems have previously been shown to exhibit mucoadhesive behavior and sustained release due to their spiny topography, including applications in bladder retention and intestinal adhesion [28, 29]. These studies highlight the potential of pollen structures for biomedical delivery, supporting the rationale of our PM-based tumor delivery platform. By sequential defatting and alkaline treatment, native pollen was transformed into negatively charged, biodegradable microgels [30, 31], which were subsequently coated with cationic liposomes to enable electrostatic assembly of Fe_3O_4 NPs, forming a PM/Lipo/NP composite [32]. This hierarchical architecture integrates natural morphology and nanoscale engineering to yield a magnetically responsive construct capable of withstanding interstitial shear within tumor tissue. The pollen-derived scaffold not only promotes NP retention but also undergoes gradual oxidative degradation under TME conditions (H_2O_2, pH 6.5), ensuring eventual clearance [33]. By coupling structural bioinspiration with lipid-mediated electrostatics and magnetic functionality, the system provides a biodegradable and durable platform for sustained magnetic hyperthermia.

In vivo, the PM/Lipo/NP composite exhibited long-term tumor retention, maintained therapeutic temperatures for over three weeks, and induced near-complete tumor regression without systemic toxicity demonstrating a new paradigm for structural bioinspiration in nanomedicine design.

2 | Results

2.1 | Design and Assembly Mechanism of PM/Lipo/NP Composites

The results describe the rational design and self-assembly mechanism of the PM/Lipo/NP composites, experimentally validated through microscopy and simulation. This characterization-supported analysis confirms that the spiky pollen morphology facilitates electrostatic assembly of cationic liposomes and Fe_3O_4 NPs, forming a uniformly coated magnetic composite. To realize this concept, sunflower pollen grains were first defatted and subjected to alkaline treatment to introduce a negatively charged surface, following a previously established protocol in our laboratory [31, 34, 35]. A cationic liposome composed of 1,2-dioleoyl-sn-glycero-3-phosphoethanolamine (DOPE) and 1,2-dipalmitoyl-3-trimethylammonium-propane chloride (DPTAP) was synthesized using our in-house technique called the liposome under cryo-assembly (LUCA) cycle method [32]. To enable surface attachment of NPs, the negatively charged PM were first coated with cationic liposomes, followed by electrostatic assembly of Fe_3O_4 NPs onto the outer surface, as illustrated in Figure 1a. The liposome-coated PMs were subsequently mixed with ultrasonicated NPs to obtain the final composite structure, PM/Lipo/NP. COMSOL Multiphysics 6.2 (Electrostatics Module) was used to simulate the surface electric field distribution of a sunflower pollen grain, representing a typical spiky morphology (Figure 1b,c). The simulation revealed a pronounced spike-dependent field enhancement, where stronger electric fields at the apex of each sunflower spike guided the preferential accumulation of liposomes and NPs during electrostatic self-assembly.

To experimentally validate the spike-dependent electric-field enhancement predicted by COMSOL simulation, we first

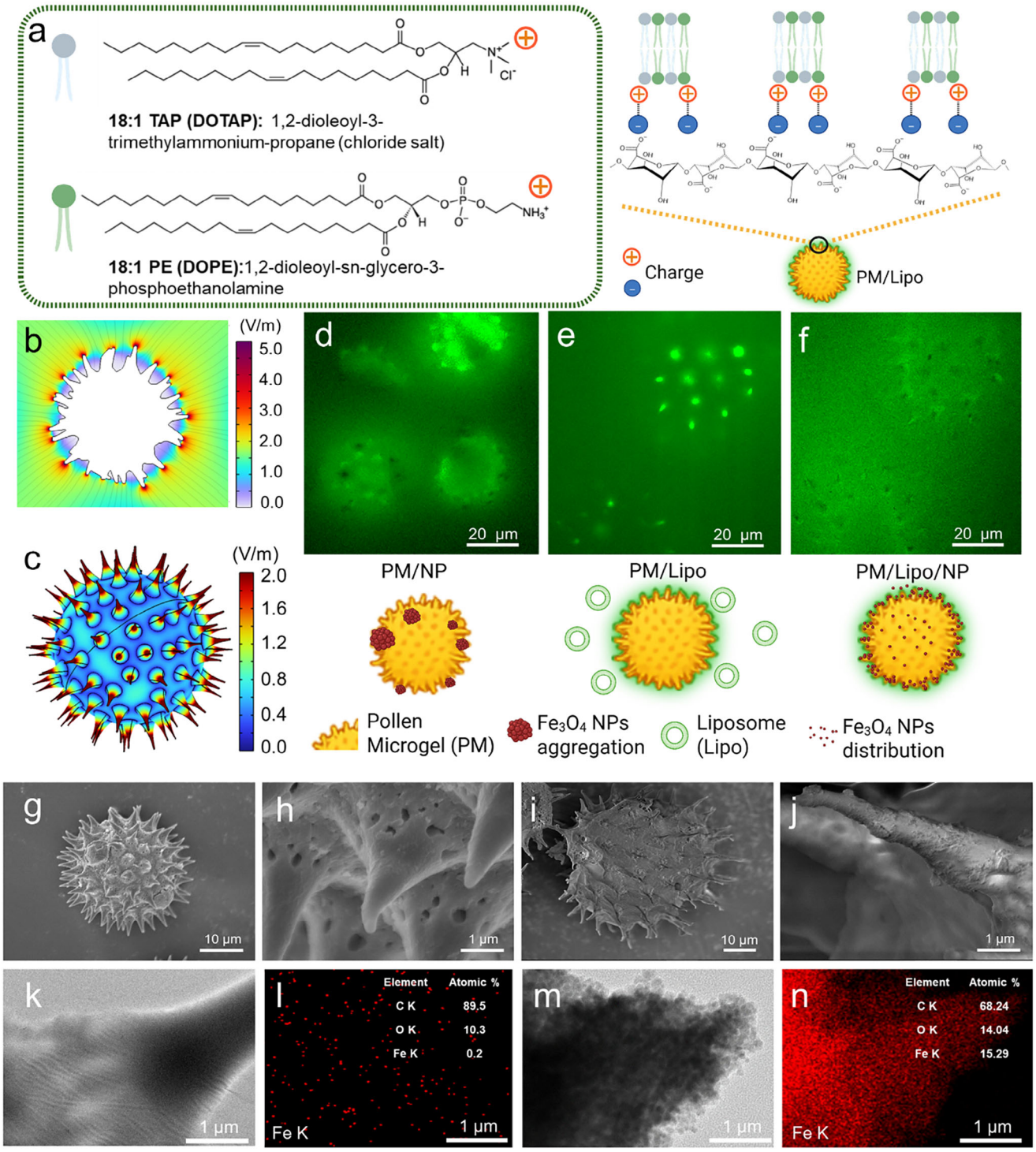

FIGURE 1 | Schematic illustration and characterization of PM/Lipo/NP composite formation. (a) Molecular structures of cationic lipids (DPTAP and DOPE) and schematic of electrostatic self-assembly between negatively charged defatted pollen microgels (PM). (b,c) COMSOL-simulated electric field distribution around spiky pollen grains, showing enhanced field intensity at spike (spike effect). (d–f) Fluorescence microscopy of PM mixed with NPs (d), FITC-labeled liposomes coated on PM (e), and PM/Lipo/NP composite (f), demonstrating spike-localized accumulation driven by electric field gradients. (g–j), SEM images showing morphology of raw pollen (g) and (h), is high-magnification view of (g) highlighting the smooth and porous spike surfaces. (i), shows PM/Lipo/NP composite and (j) is high-magnification view of (i) revealing increased surface roughness on the spike spikes after chemical treatment, liposome, and NP coating; k–m), TEM images of raw pollen (k) and (l) EDX mapping and elemental quantification of Fe in untreated pollen (k), and PM/Lipo/NP composites (m) and (n) EDX mapping indicating enhanced coated NP distribution (Fe: 15.29 at%) enabled by liposome-mediated assembly.

examined how liposomes and NPs adsorb onto the sunflower PM surface. Direct mixing of PMs and NPs without liposome mediation resulted in severe NP aggregation (Figure 1d), indicating that additional surface modification was required for controlled assembly. Therefore, fluorescently labeled liposomes (FITC-PE)-labeled liposomes were introduced to probe the effect of local field distribution. Fluorescence imaging (Figure 1e) showed stronger liposome accumulation at the spike apexes, consistent with the higher local electric field predicted by COMSOL (Figure 1b,c). Upon addition of Fe_3O_4 NPs, a similar enrichment pattern was observed (Figure 1f), supporting curvature-enhanced interaction. Importantly, this spike-localized signal represents relative preference rather than exclusive localization: the entire pollen surface remains negatively charged and capable of adsorbing liposomes and NPs, while the spike apexes having higher curvature and higher simulated field intensity display more pronounced accumulation.

The overall morphology before and after each assembly step was further examined by scanning electron microscopy (SEM) (Figure 1g–j). After defatting and alkaline treatment, the initially coarse exine spikes became slenderer, producing the characteristic spiky structure required for field-guided assembly. Transmission electron microscopy (TEM) imaging (Figure 1k,m) revealed distinct differences in internal and surface organization between untreated pollen and the final PM/Lipo/NP composite. Figure S1a,b shows that the Fe_3O_4 NPs were spherical with an average diameter of 10.6 ± 2 nm. In contrast, PM mixed directly with NPs (PM/NP) exhibited pronounced NP aggregation, as confirmed by EDX mapping (Figure S1c,d), which showed clustered Fe signals. Liposome-mediated assembly markedly improved NP distribution: untreated PM/NP exhibited negligible Fe content (0.2 at%, Figure 1l), whereas PM/Lipo/NP showed a dense and uniform NP coating with 15.29 at% Fe (Figure 1n). While EDX detects only inorganic elements and therefore cannot visualize liposomes, the Fe mapping clearly demonstrates that liposome mediation enables efficient NP loading and reduces aggregation. Together, these results confirm that spike geometry enhances NP adsorption at high-field apex regions without excluding additional attachment across the pollen surface, consistent with a curvature-dependent, electrostatically driven assembly process.

2.2 | Structural and Physicochemical Characterization of PM/Lipo/NP Composites

The PM/Lipo/NP composite was prepared through a stepwise assembly process in which surface-charge contrast played an important role. Zeta potential measurements (Figure 2a) showed that PMs possessed a highly negative surface charge (−30.1 ± 1.1 mV), whereas the cationic liposomes exhibited a strongly positive potential (+57.0 ± 1.4 mV). Their combination resulted in a PM/Lipo composite with an overall negative potential (−32.0 ± 1.0 mV), which may reflect incomplete liposome coverage or local charge heterogeneity. Fe_3O_4 NPs (−22.1 ± 0.7 mV) were subsequently incorporated, producing PM/Lipo/NP with a final potential of −43.7 ± 3.0 mV. Independent titration experiments (Figure 2b) showed that adding only 5 μL liposomes per 1 mg NP reversed the NP surface charge to +37.7 ± 1.3 mV. Collectively, these charge-shift trends are consistent with electrostatic interactions contributing to the assembly process. Increasing liposome amounts further enlarged the hydrodynamic diameter of Lipo/NP complexes, peaking at 310.4 ± 13.7 nm with 100 μL liposomes (Figure 2c), which was thus selected as the optimal ratio. NP loading onto PM/Lipo was subsequently performed under these conditions. However, excessive NP input caused aggregation and reduced loading efficiency, as confirmed by filtration-based quantification (Figure 2d).

To examine the structural and magnetic properties, X-ray diffraction (XRD), X-ray photoelectron spectroscopy (XPS), and superconducting quantum interference device (SQUID) magnetometry were performed. XRD patterns (Figure 2e) confirmed the crystalline nature of Fe_3O_4 NPs, with six characteristic peaks corresponding to (220), (311), (400), (422), (511), and (440) planes, matching the standard magnetite phase (JCPDS no. 75-0033) [36]. In contrast, PM-based samples (PM, PM/Lipo, PM/Lipo/NP) exhibited broad humps at $2\theta = 10°–20°$, indicating their amorphous nature. XPS analysis (Figure 2f) revealed Fe 2p peaks at 709.5, 711.3, 722.7, and 724.6 eV (Fe^{2+}), and 713.4 and 727.1 eV (Fe^{3+}), along with satellite features, confirming the mixed-valence state characteristic of Fe_3O_4's spinel structure. SQUID magnetometry (Figure 2g) showed a high saturation magnetization of 67.3 emu/g for Fe_3O_4 NPs, consistent with superparamagnetic behavior [37]. Although magnetization decreased to 31.8 emu/g in the PM/Lipo/NP composite due to non-magnetic components, the material retained a typical superparamagnetic hysteresis profile, supporting its suitability for magnetic hyperthermia and targeted delivery applications.

2.3 | Magnetothermal Performance and Cytocompatibility

Having established the structural and magnetic characteristics of the PM/Lipo/NP composites, we next evaluated their functional performance under alternating magnetic field (AMF) stimulation. This section examines whether the incorporated Fe_3O_4 NPs can generate homogeneous and sustained heating suitable for magnetic hyperthermia while maintaining biocompatibility in vitro. Accordingly, the magnetic responsiveness, heating efficiency, and cytocompatibility of the composites were systematically investigated. The magnetic behavior of the materials was first qualitatively confirmed using a permanent magnet (Figure 3a). While the PM alone remained unresponsive, both Fe_3O_4 NPs and PM/Lipo/NP composite rapidly aggregated toward the magnet, indicating successful magnetic incorporation into the composite system. Magnetothermal behavior was then assessed under AMF stimulation (750–1150 kHz, 300 s). Minimal heating (~36°C) was observed for PM and PM/Lipo alone, whereas PM/Lipo/NP composite containing 2 mg Fe_3O_4 NPs reached 53.2°C ± 0.2°C (Figure 3b). Remarkably, even at a reduced NP concentration of 200 μg/mL, the composite still achieved 49.1°C ± 0.2°C comparable to 400 μg/mL of pure NP demonstrating enhanced heating efficiency per unit NP (Figure S2a). Infrared (IR) thermal imaging (Figure 3c) showed a more uniform macroscopic temperature profile for the PM/Lipo/NP suspension compared with the free NP sample, which exhibited visible hotspot formation (Figure S2b). Because infrared thermography reflects bulk-level temperature distribution rather than particle-level heating, these images indicate improved overall heat dispersion in the PM/Lipo/NP group, consistent with enhanced NP

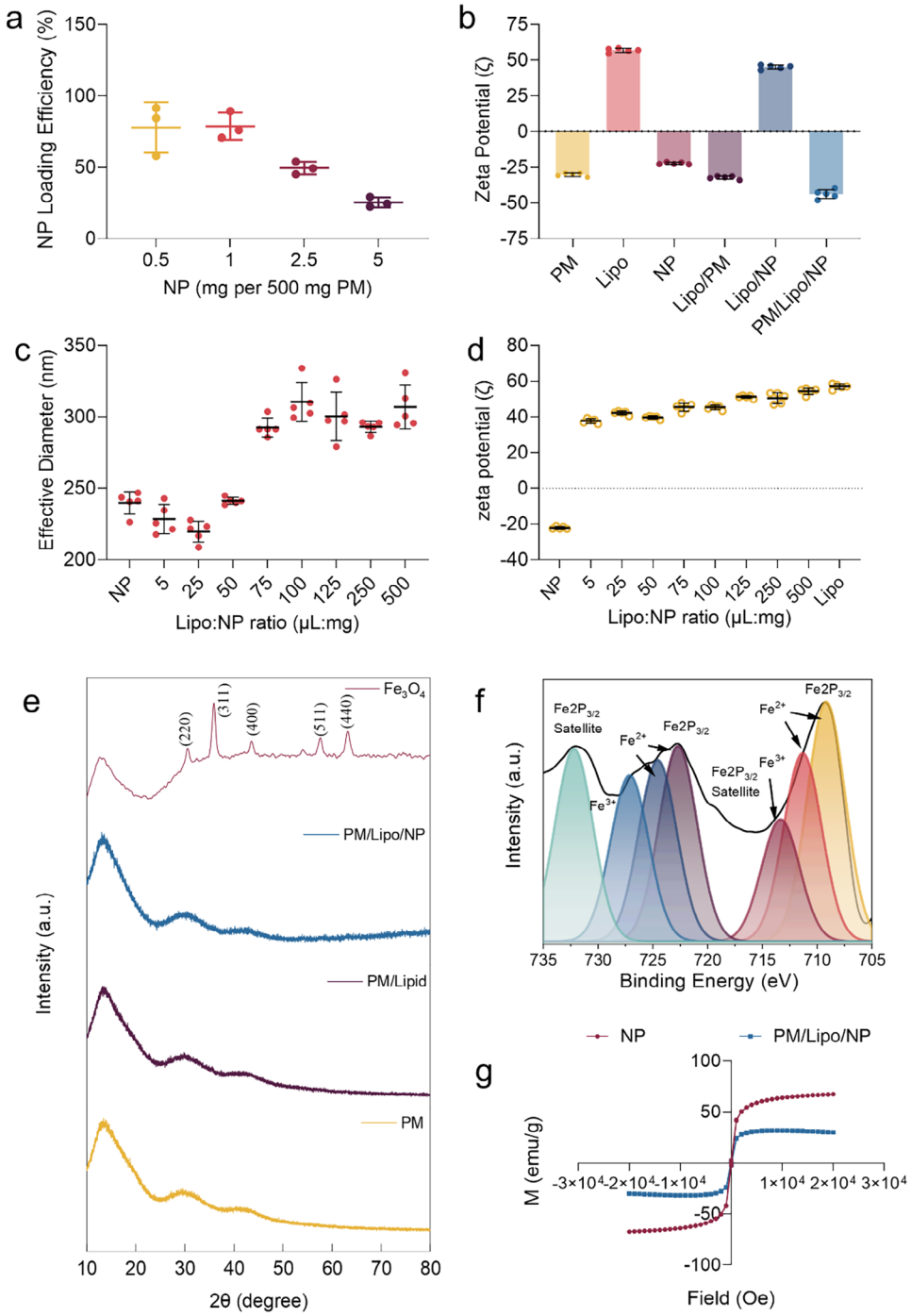

FIGURE 2 | Characterization of PM/Lipo/NP composite formation and properties. (a) Zeta potential analysis of individual components and assembled formulations confirmed electrostatic self-assembly. (b) Surface potential shift of Fe_3O_4 NPs upon liposome addition indicates charge inversion. (c) Hydrodynamic size of Lipo/NP complexes increases with liposome volume, identifying optimal complexation conditions. (d) NP loading efficiency in PM/Lipo matrix with various NP concentrations. (e) XRD patterns verify the crystalline structure of Fe_3O_4 and the amorphous nature of PM-based composites. (f) XPS confirms the presence of mixed-valence iron species in Fe_3O_4 NPs. (g) SQUID magnetometry shows superparamagnetic behavior retained after composite formation.

dispersion and more stable magnetic energy conversion within the solution.

Cytocompatibility evaluations showed that PM/Lipo/NP maintained high cell viability in the absence of AMF exposure (Figure 3d). Upon AMF treatment, however, the PM/Lipo/NP containing 200 μg/mL NP significantly reduced HepG2 cell proliferation (Figure 3e), confirming effective magnetic hyperthermia-induced cytotoxicity. This concentration was subsequently selected as the optimized condition for all following in vitro assays. To assess whether the composite also possessed chemodynamic therapeutic (CDT) potential, cell viability assays were conducted under biomimetic TME (pH 6.5) in the presence and absence of H_2O_2. As shown in Figure 3f, both PM/Lipo/NP (200 μg/mL) and free

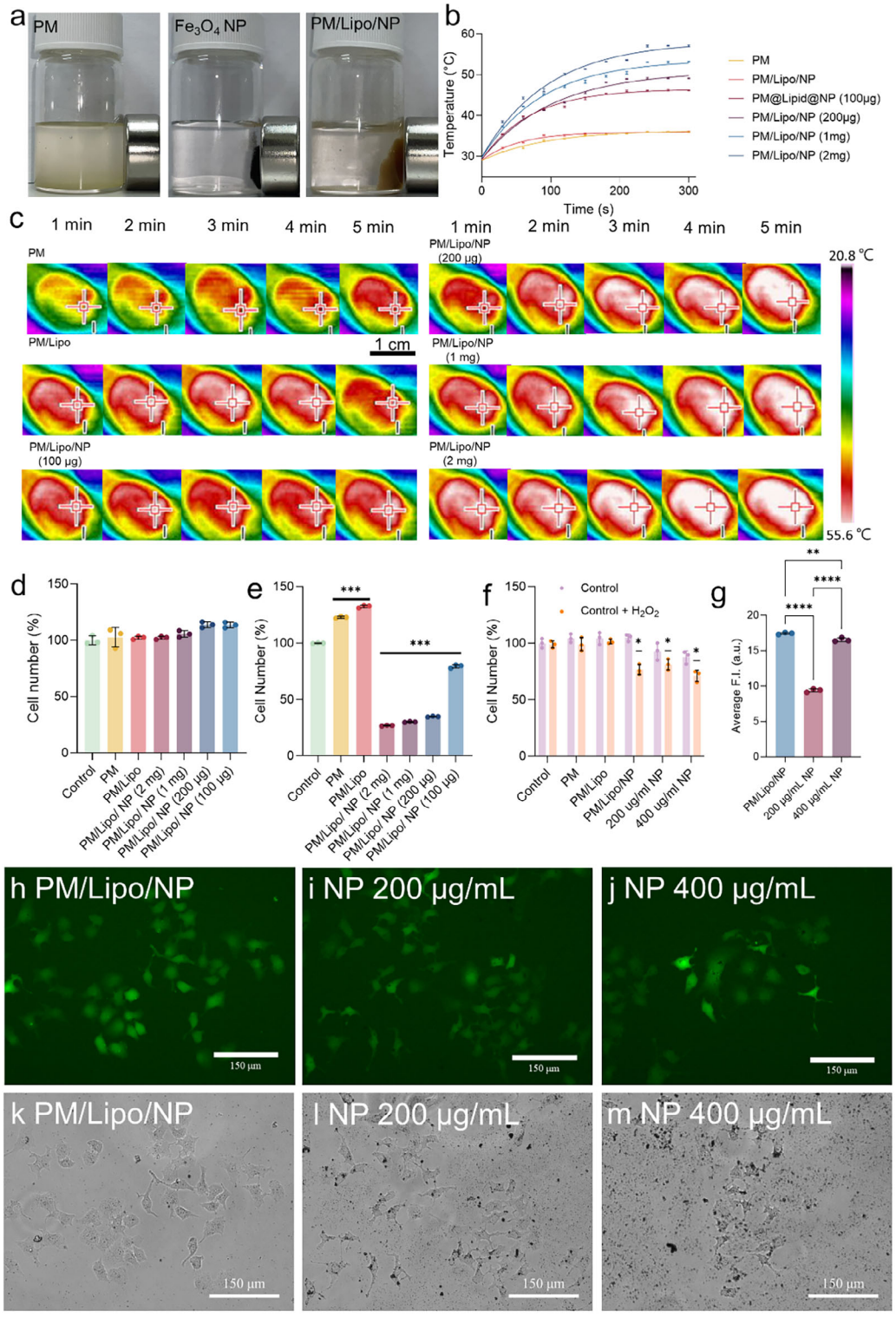

FIGURE 3 | Characterization of magnetic responsiveness, heating efficiency, cytocompatibility, chemodynamic activity, and cellular uptake of PM/Lipo/NP composites. (a) Qualitative magnet response of PM, Fe_3O_4 NPs, and PM/Lipo/NP composites under a permanent magnet. (b) Hyperthermia elevation profiles of samples under alternating magnetic field (AMF, 750–1150 KHz, 300 s), showing enhanced heating performance of PM/Lipo/NP. (c) Infrared thermal images during AMF exposure, demonstrating homogeneous heat distribution for PM/Lipo/NP compared to hot spot formation in pure NP. (d) Cell viability of HepG2 cells after 24 h incubation with different samples (non-AMF), indicating low cytotoxicity. (e) Post-AMF (750 – 1150 kHz, 300 s) viability assay showing effective magnetic hyperthermia-induced cell inhibition by PM/Lipo/NP at 200 μg/mL NP concentration. (f) Cell viability under oxidative TME-mimicking conditions (pH 6.5, H_2O_2), demonstrating comparable chemodynamic therapy (CDT) efficacy of PM/Lipo/NP and Fe_3O_4 NPs. (g) Fluorescence intensity of methylene blue (MB) degradation assay. (h–j), Fluorescence images of MB degradation assay for evaluating ROS generation by PM/Lipo/NP and Fe_3O_4 NPs, confirming similar Fenton-like activity. (k–m), Optical images showing cellular internalization of PM/Lipo/NP versus free NPs (200 and 400 μg/mL), indicating reduced NP uptake due to surface retention on the PM/Lipo carrier.

Fe_3O_4 NPs (400 μg/mL) elicited comparable inhibition of HepG2 cells (76.6 ± 4.0% and 71.2 ± 4.4%, respectively), implicating efficient CDT activity via Fenton-like reactions [38]. This was corroborated by methylene blue (MB) degradation assays (Figure 3g–j), which showed similar fluorescence quenching patterns, indicating equivalent ROS production and preserved Fe^{2+}/Fe^{3+} cycling. Finally, cellular uptake analysis revealed significantly reduced internalization of NPs in the PM/Lipo/NP group compared to free NP treatments at both 200 and 400 μg/mL (Figure 3k–m). These observations suggest that the composite effectively retained NP on the PM/Lipo carrier, limiting premature intracellular clearance and potentially enabling sustained therapeutic action. The combined benefits of enhanced colloidal stability, improved heating uniformity, reduced NP dosage, and prolonged NP retention collectively position PM/Lipo/NP as a robust and multifunctional composite for safe and efficient hyperthermia-based cancer therapy.

2.4 | Oxidative Degradation of Pollen Microgels under Tumor-Mimicking Conditions

Tumor-derived ROS play pivotal roles in cancer progression by modulating cellular survival, proliferation, and motility [39]. Among these, H_2O_2 is particularly notable due to its membrane permeability and signaling capability. The concentration of H_2O_2 varies across tumor types; for instance, HepG2 cells can release ~63 ± 0.7 nM H_2O_2 per 1×10^6 cells over several hours [39, 40]. Leveraging endogenous H_2O_2 in the TME, CDT has emerged as a promising therapeutic approach. In our system, H_2O_2 serves not only as a catalytic trigger for CDT, but also as an oxidant for pollen degradation. While pollen grains are chemically robust, their natural germination involves H_2O_2-mediated processes that initiate degradation of the sporopollenin-rich wall. Upon contact with the stigma, pollen grains adhere due to their unique exine morphology. The stigma, in turn, is enriched with antioxidants, peroxidases, and H_2O_2, which initiate biochemical processes that degrade even the highly resistant sporopollenin layer of the pollen wall [33]. To mimic this oxidative susceptibility, we exposed PM to 100 mM H_2O_2 at pH 6.5. A schematic overview (Figure 4a) illustrates the progressive morphological transformation under oxidative conditions. Optical microscopy (Figure 4b) and SEM (Figure 4c) reveal a gradual transition from spiky, intact microgels to aggregated and fragmented debris, indicating structural disintegration of the exine.

Quantitative analysis of degradation was conducted using dry weight loss, Auramine O fluorescence, and FTIR spectroscopy. As shown in Figure 4d, PM exhibited a 65% reduction in residual weight, consistent with extensive material degradation. Concurrently, Auramine O fluorescence decreased by 57% (Figure 4e), reflecting disruption of π-conjugated and hydrophobic domains within sporopollenin to which the dye binds [41]; the fluorescence loss suggests structural cleavage of these regions, supporting its use as a sensitive indicator of exine degradation under H_2O_2 treatment [41]. FTIR analysis from days 0 to 21 (Figure 4f) further confirmed chemical breakdown. The aromatic C—H bending peak at 846 cm^{-1} diminished steadily, along with the C=C stretching bands at 1500 and 1580 cm^{-1}, indicating cleavage of phenolic and aromatic units [42]. Decreases in the 1100 cm^{-1} peak (C—O—C and C—O stretching) suggest breakdown of ether and ester linkages stabilizing the sporopollenin backbone. Simultaneously, new signals at 2990, 3300, and 3680 cm^{-1} emerged, corresponding to aliphatic C—H and hydroxyl stretching vibrations, implying the formation of hydroxylated, polar degradation products such as alcohols, phenolics, and carboxylic acids. The increase in $\delta(CH_2)n$ signal at 777 cm^{-1} may reflect unmasking or reorganization of internal aromatic substructures during matrix oxidation [43]. Together, these findings demonstrate that H_2O_2 exposure under TME-mimicking conditions induces progressive cleavage of both aromatic and aliphatic domains in the sporopollenin matrix. This degradation enhances surface polarity, reduces material integrity, and may facilitate subsequent chemical functionalization or therapeutic payload incorporation. While these results confirm the oxidative degradability of PM under simplified TME conditions, it is important to note that in vivo degradation is likely governed by a more complex interplay of mechanisms, including cellular uptake, enzymatic activity, and phagocytic clearance, which may further modulate the biodegradation profile of the pollen-based carrier system.

2.5 | In Vivo Tumor Retention and Therapeutic Efficacy

The in vivo therapeutic efficacy and biosafety of the PM/Lipo/NP composite were assessed using a subcutaneous tumor model in Sprague-Dawley rats. Thermal imaging on day 1 (Figure 5a) confirmed effective heat generation in both the free NP and PM/Lipo/NP groups under AMF stimulation. However, while the free NP group exhibited a sharp decline in heating by day 7, the PM/Lipo/NP composite maintained stable, localized heating over 21 days. Notably, the burn area in free NP-treated rats reached 1.56 ± 0.08 cm^2 significantly larger than the 0.27 ± 0.05 cm^2 observed in the PM/Lipo/NP group (Figure S3) indicative of uncontrolled NP dispersion and off-target heating. Tumor images harvested after 21 days (Figure 5b) showed near-complete regression in the PM/Lipo/NP group, with tumors nearly unharvestable upon visual inspection. In contrast, although free NPs reduced tumor volume, thermal damage in early stages complicated assessment. Body weight remained stable across all groups (Figure 5c,f), suggesting good systemic tolerability. Thermal stability profiles (Figure 5d,g) further highlighted the retention advantage of PM/Lipo/NP; therapeutic temperatures were sustained (48.0°C ± 0.7°C on day 0; 44.9°C ± 0.3°C on Day 21), while free NP samples dropped below 40.0°C by day 5, consistent with poor tumor retention and rapid clearance. Serial tumor size tracking (Figure 5e,h) demonstrated continuous tumor regression in the PM/Lipo/NP group, whereas the free NP group showed delayed shrinkage following eschar detachment again reflecting limited NP persistence. These findings emphasize the clinical relevance of retention stability. While single-session magnetic hyperthermia may be effective in preclinical settings, repeated dosing is typically required in patients. NP systems with poor intratumoral retention and off-target distribution pose translational challenges and safety concerns.

Histological examination (Figure 5i) supported these observations. Control, PM, and PM/Lipo groups preserved tumor histoarchitecture, while both NP and PM/Lipo/NP groups exhibited extensive tumor cell damage and fibrotic remodeling. Importantly, systemic toxicity assessments (Figure S4) revealed no

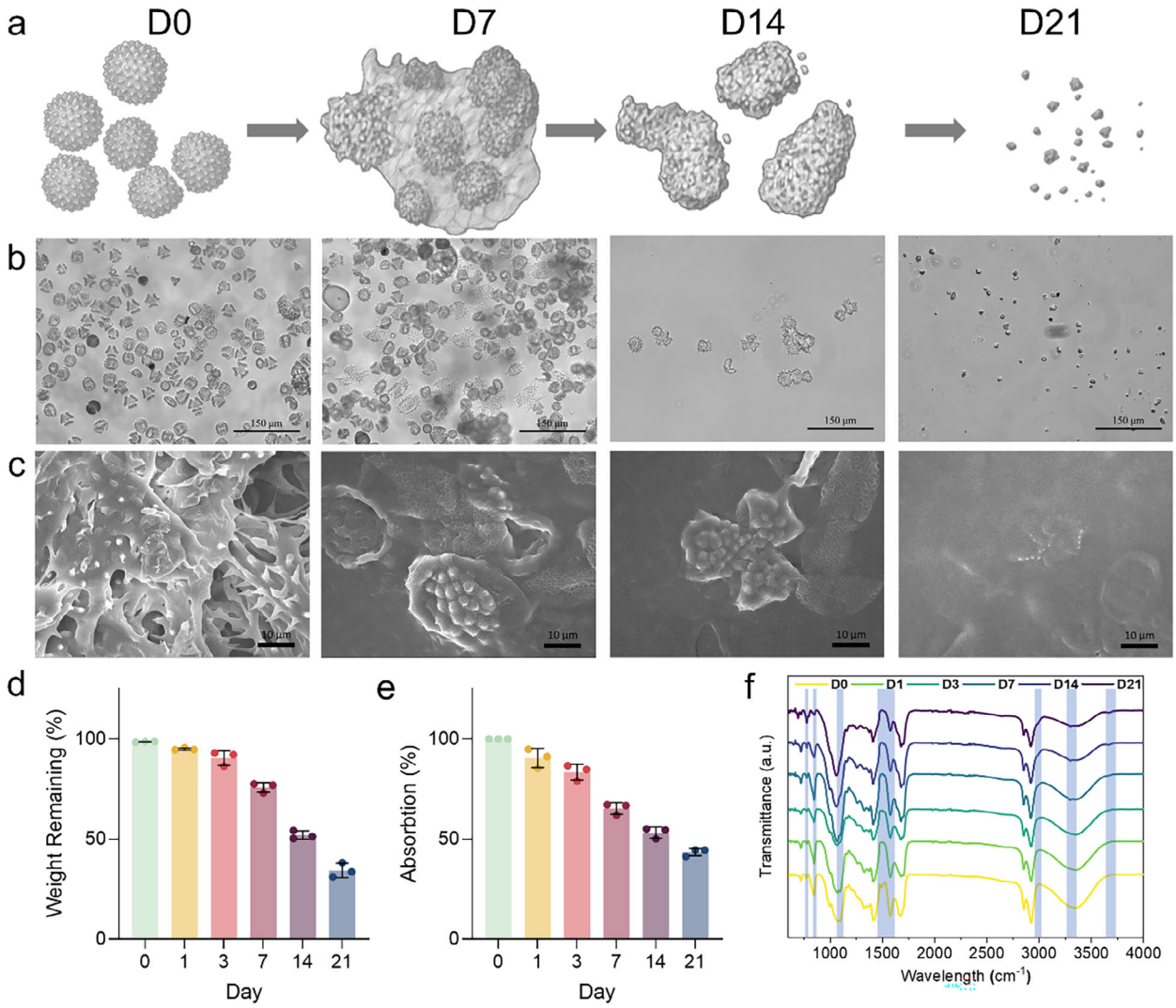

FIGURE 4 | Evaluation of H_2O_2-induced degradation of PM under TME-mimicking conditions (1 mg PM in 100 mM H_2O_2, pH 6.5). (a) Schematic illustration of stepwise PM degradation: from intact morphology to aggregation, fragmentation, and complete disintegration. (b) Optical microscopy images showing morphological changes in PM during degradation. (c) SEM images confirming progressive collapse of the exine layer and loss of structural integrity. (d) Residual dry weight of PM samples over time, indicating a 65% reduction after 21 days. (e) Auramine O fluorescence intensity decreased by 57%, reflecting cleavage of π-conjugated and hydrophobic domains within sporopollenin. (f) FTIR spectra collected from days 0 to 21 showing progressive chemical changes during ROS-mediated degradation of PM/Lipo/NP composites. The highlighted blue regions (from left to right: 777, 846, 1100, 1500, 1580, 2990, 3300, and 3680 cm^{-1}) indicate key vibrational bands that undergo characteristic shifts or intensity loss over time.

inflammation or lesions in major organs, and blood biochemical markers (AST, ALT, BUN, CRE; Table S1) [44] remained within physiological limits, confirming the biosafety of the PM-based formulation. No residual pollen debris or adverse effects were detected. Taken together, these results confirm that the PM/Lipo/NP composite achieves effective and sustained magnetic hyperthermia, with enhanced tumor retention, minimized off-target effects, and excellent in vivo biosafety. This highlights the potential of pollen-based carriers as a clinically translatable, bioinspired alternative for localized long-term cancer therapy.

3 | Discussion

The design of our composite draws inspiration from the evolutionary role of pollen grains as specialized adhesive carriers. In plants, the spiny exine morphology enhances anchorage to the stigma, improving pollination efficiency in dynamic environments [27]. To validate the role of the spiny structure in enhancing particle accumulation, a monolayer cell flushing assay demonstrated that spiky sunflower pollen exhibited approximately a 6.7-fold increase in accumulation compared to smooth camellia pollen (Figure S5). This observation is consistent with previous findings showing that sunflower pollen has a 12.5-fold higher wash-off resistance than spherical particles under shear stress conditions [27]. Repurposing this architecture, we engineered sunflower-derived microgels with microscale dimensions and nanoscale spike that promote passive tumor retention via shape-induced interlocking. This physical anchoring mechanism provides a receptor-independent strategy for resisting interstitial shear and enhancing localization within the tumor matrix offering potential advantages over conventional ligand–receptor

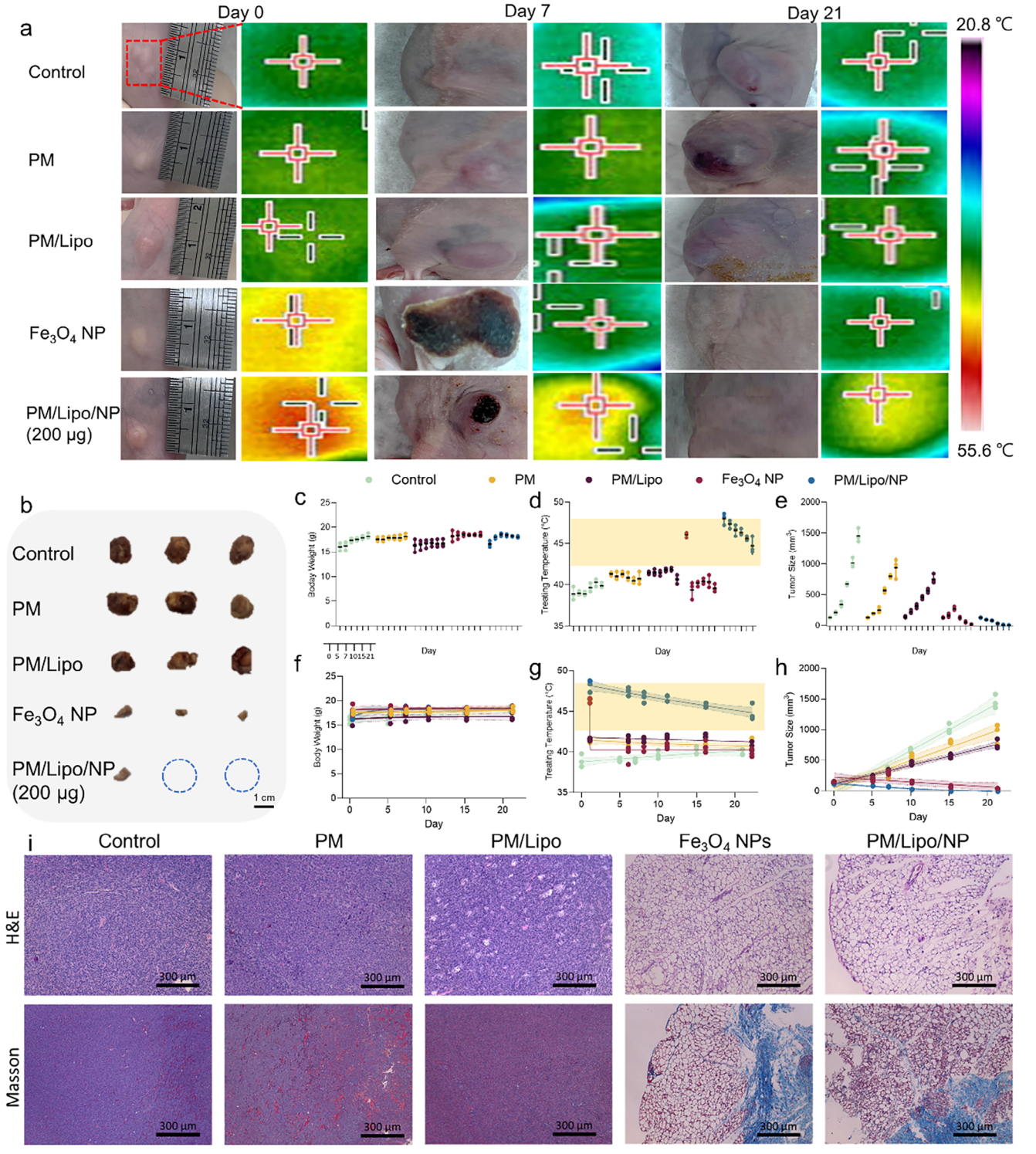

FIGURE 5 | In vivo evaluation of magnetic hyperthermia efficacy and biosafety using a subcutaneous tumor model in SD rats. (a) Representative thermal images during AMF treatment on days 0, 7, and 21 showing consistent and localized heating in the PM/Lipo/NP group, and loss of heating in the free NP group. (b) Optical images of excised tumors after 21-day treatment; PM/Lipo/NP group exhibited near-complete tumor regression. (c) Body weight monitoring over time; (f), corresponding confidence intervals for (c), indicating no significant systemic toxicity across all groups. (d) Treatment temperature profiles during AMF exposure on each treatment day; (g) corresponding confidence intervals for (d), highlighting therapeutic heating range. (e) Tumor volume observation over time; (h) corresponding confidence intervals for (e), demonstrating consistent antitumor efficacy in the PM/Lipo/NP group. (i) H&E and Masson's trichrome staining of tumor tissues after 21 days, showing structural preservation in control, PM, and PM/Lipo groups, and extensive tumor degradation and fibrosis in NP and PM/Lipo/NP groups.

targeting, which is often compromised by tumor heterogeneity [45].

To further align with tumor-specific features, we leveraged the elevated ROS levels in the TME as functional triggers. H_2O_2 acts both as a catalytic co-factor for CDT and as a degradation stimulus for the PM scaffold. While sporopollenin is known for its chemical robustness, exposure to oxidative conditions initiates its gradual fragmentation, enabling a transition from retention to clearance [33]. Interestingly, this mechanism parallels the natural pollen germination process, where high H_2O_2 levels are also found near the plant stigma and contribute to exine loosening and pollen tube emergence [46]. In addition to these physicochemical interactions, the spiny pollen-derived architecture may also influence local immune responses. Recent studies have shown that sunflower-derived sporopollenin capsules can strongly interact with macrophages, promote phagocytic uptake, and even modulate macrophage polarization through spike-mediated mechanical stimulation [47]. Such immune engagement suggests that the PM carrier could participate not only in geometry-guided retention but also in immune-assisted tumor suppression, although the primary therapeutic effect in this work derives from hyperthermia. While comprehensive immunological profiling is beyond the scope of the present study, these findings highlight the potential contribution of macrophage–pollen interactions and point to immune-modulatory mechanisms as an important avenue for future investigation.

Beyond their adhesive and immune-interactive characteristics, the TME-responsive degradability of PMs positions them within a broader category of pathologically responsive hydrogels, which have recently shown great promise in controlled drug delivery, immunomodulation, and adaptive therapeutic systems [48]. ROS- or acidity-responsive hydrogels have been engineered to undergo structural softening, fragmentation, or on-demand release in diseased tissues, enabling spatiotemporally controlled therapeutic action [49]. The gradual degradation of PMs under tumor-relevant oxidative and mildly acidic conditions mirrors these design principles, but with the unique advantage of originating from a naturally derived, structurally encoded microgel system rather than a synthetically engineered polymer. This positions PM as a distinctive, bioinspired analogue to synthetic smart hydrogels capable of transitioning from mechanically anchored carriers to biodegradable carriers in response to pathological cues [50]. Collectively, the integration of bioinspired morphology and TME-responsive degradation offers a multifunctional strategy that enhances tumor accumulation and prolongs NP retention in magnetic hyperthermia. This approach may be broadly applicable to localized therapies requiring controllable residence and biodegradation.

4 | Conclusions

This study demonstrates that sunflower-derived PM can serve as a biodegradable, structurally defined carrier that enables long-term intratumoral retention and sustained magnetic hyperthermia. By integrating geometry-guided anchorage with TME-responsive degradation, the PM/Lipo/NP system overcomes key limitations of conventional NP therapies, achieving durable therapeutic heating and effective tumor regression with minimal systemic toxicity. The inherent TME-responsiveness of the pollen matrix, together with its natural microgel architecture, highlights the broader potential of pollen-derived materials as versatile and environmentally adaptive platforms for localized cancer treatment and other biomedical applications requiring controllable residence and safe biodegradation.

5 | Experimental Section

5.1 | Pollen Microgel Preparation

PMs were prepared using sunflower (Helianthus annuus L.) pollen obtained from Greer Laboratories, Inc. (Lenoir, NC, USA), following a previously established protocol with slight modifications [31]. In brief, the preparation involved three major steps: defatting, cytoplasmic removal, and alkaline softening. For defatting, 250 g of bee pollen granules were refluxed in 500 mL of acetone at 50°C for 3 h under magnetic stirring (220 rpm). After removing the acetone, the sample was washed with 1 L of deionized water at 50°C for 1 h, sequentially filtered through a 300 μm nylon mesh and a 6 μm filter paper under vacuum, and subsequently rehydrated in another 1 L of deionized water at 50°C for 30 min. The pollen was then subjected to a second reflux in 500 mL of acetone (50°C, 3 h), followed by vacuum filtration and air-drying in a fume hood for 12 h. The dried pollen (20 g) was further stirred in 250 mL of diethyl ether at 25°C (400 rpm) for 2 h, a step repeated twice using fresh solvent each time. To ensure complete removal of lipid residues, the pollen was stirred overnight in fresh diethyl ether under the same conditions, followed by vacuum filtration and air-drying in a fume hood for an additional 12 h. For cytoplasmic removal, 2 g of defatted pollen was mixed with 20 mL of 10% (w/v) aqueous KOH and refluxed at 80°C for 2 h under magnetic stirring. The resulting suspension was centrifuged at 5000 × g for 5 min, and the pellet was washed five times with fresh 10% KOH by vortexing for 2 min and centrifuging at 5000 × g for 5 min in each cycle. The final step involved microgel formation by resuspending the KOH-treated pollen in 40 mL of fresh 10% KOH, followed by vortexing for 2 min and static incubation at 80°C for 3, 6, or 12 h, depending on the desired degree of softening. After incubation, the pollen was centrifuged (5000 × g, 5 min), and the pellet was washed repeatedly with deionized water (vortexed 2 min, centrifuged 5 min) until the pH of the supernatant reached approximately 7.5, as determined using pH-indicator strips (MilliporeSigma, Burlington, MA, USA). The resulting pollen microgels were stored at 4°C for further characterization.

5.2 | Preparation of Liposome

Reagents. 1,2-Dioleoyl-3-trimethylammonium-propane (chloride salt) (DOTAP), 1,2-di(9Z-octadecenoyl)-sn-glycero-3-phosphoethanolamine (DOPE), and 1,2-dioleoylsn-glycero-3-phosphoethanolamine-N-(lissamine rhodamine B sulfonyl) (ammonium salt) (Rh-PE, red) lipids dissolved in chloroform were acquired from Avanti Polar Lipids (Alabaster, AL). Fluorescein DHPE (N-(Fluorescein-5-Thiocarbamoyl)-1,2-Dihexadecanoyl-sn-Glycero-3-Phosphoethanolamine, Triethylammonium Salt) (FITC-PE, green) lipid in power form was

obtained from Thermo Fisher Scientific (Waltham, MA). The buffer used in all experiments was Milli-Q water (MilliporeSigma, Burlington, MA).

Liposome Preparation. Positively charged liposomes were prepared using the thin film hydration method, followed by a liposome under cryo-assembly (LUCA) cycle [32, 51]. Initially, predetermined amounts of cationic DOTAP and neutral DOPE lipids in chloroform were mixed in a glass vial. The solvent was then evaporated under a gentle nitrogen gas flow and subsequent overnight drying in a vacuum desiccator. Unless specified otherwise, the molar ratio of DOTAP and DOPE was maintained at 1:1. For fluorescence experiments, Rh-PE or FITC-PE was incorporated at 0.5 mol% in place of an equivalent fraction of DOPE. For example, in liposomes containing Rh-PE, the composition consisted of 50.0 mol% DOTAP, 49.5 mol% DOPE, and 0.5 mol% Rh-PE. Next, the dried lipid film was hydrated by vortexing in Milli-Q water or UltraPure DNase/RNase-free distilled water (Thermo Fisher Scientific, Waltham, MA). The resulting lipid suspension then underwent five LUCA cycles, which included sequential steps of: (1) immersion in liquid nitrogen for 1 min, (2) thawing in a 60°C water bath for 5 min, and (3) vortexing for 30 s. Unless otherwise noted, the final lipid concentration was fixed at 20 mM.

5.3 | Preparation of Fe_3O_4 Nanoparticles

Fe_3O_4 nanoparticles (NPs) were synthesized via a co-precipitation method. Briefly, 5.84 g of $FeCl_3{\cdot}6H_2O$ and 2.15 g of $FeCl_2{\cdot}4H_2O$ (Sigma-Aldrich, USA) were dissolved in 100 mL of deionized water in a three-neck flask. The mixture was stirred at 1200 rpm under a nitrogen atmosphere while gradually heating. Once the temperature reached 60°C, 30 mL of 25% ammonium hydroxide solution was added dropwise [52]. The reaction was maintained for 1 h, during which a black precipitate formed. The Fe_3O_4 NPs were collected using an external magnet and washed several times with deionized water and ethanol. The final product was vacuum-dried at 60°C for 12 h.

5.4 | Preparation of PM/Lipo/NP Composite

The PM/Lipo/NP composite was prepared via electrostatic self-assembly. First, 100 mg of PM were dispersed in 1 mL of deionized (DI) water by vortexing for 30 s. Subsequently, 100 µL of 20 mM cationic liposome solution was added, followed by another 30 s of vortexing. The mixture was centrifuged at 350 × g for 3 min to remove the supernatant, and the pellet was re-dispersed in 1 mL of deionized water to obtain the PM/Lipo solution. Separately, Fe_3O_4 NPs were ultrasonicated for 10 min to ensure uniform dispersion at a concentration of 200 µg/mL. The Fe_3O_4 NP solution was then added to the PM/Lipo dispersion and vortexed for 30s. A permanent magnet was placed adjacent to the tube to collect the magnetically responsive PM/Lipo/NP composites, and the supernatant containing unbound particles was removed. To further purify the composite, the sample was filtered using a 10 µm mesh cell strainer to eliminate non-assembled NPs. The final product was centrifuged and resuspended in fresh dispersion medium for further use.

5.5 | Pollen Surface Electrostatic Simulation

In electrostatic equilibrium [53, 54], the surface charge density (σ) on a conductor is directly proportional to the magnitude of the local surface electric field (E), as expressed in Equation (1). Moreover, due to the well-known tip effect, the magnitude of the electric field at a point on a conductor's surface is inversely proportional to the local radius of curvature (r), as described by Equation (2). As a result, sharp protrusions (regions with small r) accumulate higher surface charge densities and exhibit correspondingly stronger electric fields, whereas flatter areas (large r) exhibit lower charge densities and weaker fields.

In this study, COMSOL Multiphysics 6.2 (Electrostatics Module) is used to numerically simulate the surface electric field distribution on a model of a sunflower pollen particle, which is a representative example of a spiky surface. The sunflower pollen particle is modeled as a hollow structure (free charge will move around the spiky surface) embedded in a cubic air domain with a relative permittivity of embedded in a cubic air domain with a relative permittivity of $\varepsilon = 1$ (see Table S2 for specific parameters). A uniform space charge density is applied to the air domain. Under electrostatic forces, the free charges in the air domain will move. By solving the governing equation for the electric potential distribution in the system is Poisson's equation for free charge [55] (Equation 3), the distribution of the surface charge surface electric field around the spiky pollen surface will be obtained.

In the computational setup, the surface of the pollen particle is assigned a grounded boundary condition (0 V), as illustrated in Figure S6. A uniform space charge density of -1.0×10^{-6} C/m^3 is applied throughout the surrounding air domain. A free tetrahedral mesh is applied to the 3D model, with a minimum element size of 0.05 um. A stationary study is then performed to solve for the resulting electric field distribution on the pollen surface. The simulation results corroborate the theoretical prediction of the spiky effect as illustrated in Figure S7: the spiky protrusions on the pollen surface, characterized by small radii of curvature, display significantly elevated electric field magnitudes compared to the smoother, flatter regions. This outcome confirms the expected concentration of surface charge on sharp conductive features.

$$\sigma = \varepsilon_0 \mathrm{E} \tag{1}$$

$$\mathrm{E} \propto \frac{1}{\mathrm{r}} \tag{2}$$

$$\begin{cases} \nabla^2 \mathrm{V} = \frac{\rho_0}{\varepsilon} \\ \mathrm{V_o} = 0 \end{cases} \tag{3}$$

where ρ_0 is the free charge density (C/m^3), $\varepsilon = \varepsilon_r \varepsilon_0$ is the absolute permittivity of the medium, ε_r is the relative permittivity of the medium ($\varepsilon_r = 1$ for air), ε_0 is the vacuum permittivity (8.58×10^{-12}F/m), V_0 is the boundary condition of pollen surface (ground). The COMSOL model provides qualitative visualization of the field-distribution pattern rather than quantitative predictions of absolute field strength.

5.6 | Characterization of the PM/Lipo/NP Composite

NP loading efficiency was determined by quantifying the amount of Fe_3O_4 NPs incorporated into the PM/Lipo/NP composites. PM/Lipo composites were first prepared according to the procedure described in Section 5.4. For loading experiments, 500 mg of PM/Lipo composite was transferred into individual tubes and mixed with Fe_3O_4 NPs at final NP masses of 0.5, 1, 2.5, and 5 mg. Each composite was ultrasonicated for 30 min to facilitate NP loading onto the composite surface. Following assembly, the suspension was passed through a 10 μm mesh cell strainer to separate the PM/Lipo/NP composite from unbound NPs. The filtrate was collected, and the residual Fe_3O_4 content was quantified gravimetrically by drying and weighing the remaining NPs. NP loading efficiency was calculated by comparing the initial amount of NPs added with the mass of unloaded NPs recovered in the filtrate (Equation 4). The net increase in the mass of the PM/Lipo/NP composite was also recorded to confirm NP incorporation.

$$\text{Loading efficiency } (\%) = \frac{Weight_{NP\ added} - Weight_{NP\ unloaded}}{Weight_{NP\ added}} \times 100\% \quad (4)$$

The surface morphology and microstructure of PM were examined using field emission scanning electron microscopy (FESEM, JSM-7600F with TED and EBL, JEOL, Japan) after sputter-coating the samples with gold. The distribution of nanoparticles (NPs) on PM and their elemental composition were evaluated by transmission electron microscopy (TEM, JEM-2100F, JEOL, Japan) and energy-dispersive X-ray spectroscopy (EDX, S-3000H, Hitachi, Japan), respectively.

To characterize the surface properties of the PM/Lipo/NP composite, dynamic light scattering (DLS) and zeta potential measurements were conducted using a 90Plus Particle Size/Zeta PALS Analyzer (Brookhaven Instruments Corporation, NY, USA). DLS measurements were performed at a 90° scattering angle to minimize reflection artifacts, and the autocorrelation functions were analyzed using the non-negative least squares (NNLS) method.

The crystalline structure of the materials was analyzed by X-ray diffraction (XRD, X'Pert^3 Powder, Malvern PANalytical, Netherlands), while the elemental composition and chemical states of Fe_3O_4 nanoparticles were characterized using X-ray photoelectron spectroscopy (XPS, PHI 5000 VersaProbe III, ULVAC-PHI, Japan). Magnetic properties of the Fe_3O_4 NPs and the PM/Lipo/NP composite were assessed using a superconducting quantum interference device (SQUID, MPMS 3 DC, Quantum Design, USA).

To identify the functional groups and degradation products of PM, attenuated total reflection Fourier-transform infrared spectroscopy (ATR-FTIR, Spotlight 200i Sp2 with AutoATR System, PerkinElmer, USA) was performed in the spectral range of 4000–500 cm^{-1}. In addition, proton nuclear magnetic resonance spectroscopy (^{1}H NMR, 400 MHz Spectrometer, JEOL, Japan) was conducted to detect changes in the chemical structure. For NMR analysis, samples were dissolved in deuterated methanol (CD_3OD).

5.7 | Magnetic Hyperthermia Evaluation

Magnetic hyperthermia performance was evaluated using Fe_3O_4 nanoparticles at concentrations of 200, 300, and 400 μg/mL, as well as PM/Lipo/NP composites containing Fe_3O_4 at concentrations of 100 μg/mL, 200 μg/mL, 1 mg/mL, and 2 mg/mL. Samples were subjected to an alternating magnetic field (AMF) at a frequency range of 750–1150 kHz for 300s using a High-ER Frequency Induction Heater (45/900, President Honor Industries Co., Ltd., Taiwan). Temperature elevation was recorded every minute using an infrared (IR) thermal imaging camera (F30, Ching Hsing Computer-Tech Ltd., Taiwan) to generate heating profiles.

For in vivo experiments, PM/Lipo/NP composites containing 200 μg/mL of Fe_3O_4 NPs were used. AMF parameters were kept consistent with those applied in the in vitro evaluations.

5.8 | In Vitro Cytotoxicity and Magnetic Hyperthermia Evaluation

The human hepatocellular carcinoma cell line HepG2 was used in this study. Cells were cultured in Dulbecco's Modified Eagle Medium (DMEM) supplemented with 10% fetal bovine serum (FBS) and 1% penicillin/streptomycin, and maintained at 37°C in a humidified incubator with 5% CO_2.

Cytotoxicity was evaluated using the Cell Counting Kit-8 (CCK-8) assay. Briefly, HepG2 cells were seeded at a density of 1×10^4 cells per well in 96-well plates and incubated for 24 h. Various concentrations of test samples were prepared in DMEM and incubated at 37°C for 2 h before use. Then, 200 μL of each sample solution was added to the corresponding wells and incubated for an additional 24 h. Afterward, 10 μL of CCK-8 reagent was added to each well and incubated for 1 h. The absorbance was measured at 450 nm using a microplate reader (Infinite 200 PRO, TECAN, Japan). Cell viability (%) was calculated based on the relative absorbance compared to the control group (Equation 5).

$$\text{Cell viability } (\%) = \frac{(Absorbance\ of\ experiemental\ group - Absorbance\ of\ blank)}{(Absorbance\ of\ control - Absorbance\ of\ blank)} \times 100\% \quad (5)$$

For magnetic hyperthermia-assisted cancer therapy evaluation, HepG2 cells were seeded and pre-incubated for 24 h. Then, 200 μL of the sample solution was added to each well and exposed to an alternating magnetic field (AMF) generated by a 3.2 kW induction system operating at 700–1100 kHz. The AMF exposure was applied for 300 s under the same conditions used in the in vitro heating experiments. After AMF treatment, plates were incubated for an additional 24 h, and cell viability was quantified using the CCK-8 assay described above to assess magnetic hyperthermia-induced cytotoxicity.

5.9 | Chemical Dynamic Therapy: In Vitro Anticancer and ROS Generation Evaluation

To simulate the tumor microenvironment (TME), a modified culture medium was prepared by adjusting the pH to 6.5 using 100 mM H_2O_2. Different concentrations of test samples were co-incubated with HepG2 cells following the procedure described in the in vitro cytotoxicity and magnetic hyperthermia evaluation section, with the only modification being the use of the TME-mimicking medium during the 24-h incubation with the samples. After incubation, cell viability was assessed using the CCK-8 assay, as previously described.

For evaluation of reactive oxygen species (ROS) generation, methylene blue (MB) was used as a ROS-sensitive dye. A working solution of 20 μg/mL MB was added to each sample and incubated for 30 min at 37°C under standard cell culture conditions and washed using PBS for three time ready for observation. The extent of MB degradation was used as an indicator of ROS production. Fluorescence images were captured using a fluorescence microscope (EVOS M5000 Imaging System, Thermo Fisher Scientific, USA), and ROS levels were quantified based on fluorescence intensity using ImageJ software. Additionally, HepG2 cells were seeded at a density of 1×10^4 cells/mL into six-well plates and cultured for 24 h to allow cell attachment. After incubation, the culture medium was replaced with treatment media containing equivalent amounts of Fe_3O_4 NPs to ensure dose-matched comparison across groups. For the PM/Lipo/NP condition, 100 mg of PM/Lipo/NP composites containing 1 mg Fe_3O_4 NPs were dispersed in 1 mL of culture medium according to Section 5.4, yielding a final NP concentration of 200 μg/mL. For free NP controls, 1 mg or 2 mg of Fe_3O_4 NPs were dispersed in 1 mL of culture medium and ultrasonicated for 30 min to obtain stable suspensions. After sonication, the NP-containing supernatants were collected, and 200 μL of the suspension was mixed with 800 μL of fresh culture medium, resulting in final NP concentrations of 200 μg/mL (1 mg NP input) and 400 μg/mL (2 mg NP input), respectively. These dose-matched treatments were then added to the wells to ensure consistent and controlled NP exposure across all experimental groups. Cells were then co-incubated with the samples for 24 h under standard culture conditions (37°C, 5% CO_2). After treatment, the medium was removed and the cells were washed three times with PBS to eliminate non-internalized or loosely particles. Bright-field microscopy was subsequently performed to visualize cellular uptake under dose-matched conditions.

5.10 | PM In Vitro Degradation Evaluation

To simulate the TME, a modified culture medium was prepared by adjusting the pH to 6.5 using 100 mM H_2O_2. A total of 10 mg of PM-based samples were immersed in 5mL of the modified medium and incubated at 37°C with gentle orbital shaking at 50 rpm for various time points (0, 1, 3, 7, 14, and 21 days).

At each time point, samples were collected for analysis. Optical photographs were first taken to observe morphological changes during degradation. The samples were then filtered using a 10 μm mesh cell strainer to separate the degraded fragments (soluble products) from the remaining intact PM. The undegraded PM fraction was dried in a 70°C oven and weighed to assess mass loss over time.

To evaluate the degradation of sporopollenin, the collected degradation solutions were reacted with Auramine O dye, and the fluorescence intensity was measured to quantify the extent of structural breakdown. The UV–vis absorption of Auramine O was measured at 438 nm. Additionally, the dried PM residues were subjected to SEM to observe surface morphology changes, and FTIR was used to analyze the evolution of functional groups changes during degradation.

5.11 | Animal Test

All animal experiments were conducted in accordance with the guidelines approved by the Institutional Animal Care and Use Committee of Taipei Medical University (Approval No. LAC2022-0445). Six-week-old male Sprague Dawley (SD) rats were used and randomly divided into five groups: (1) control (untreated), (2) PM, (3) PM/Lipo, (4) Fe_3O_4 NP, and (5) PM/Lipo/NP (containing 200 μg/mL of Fe_3O_4 NPs).

Anesthetic solution was prepared by mixing Zoletil 50 and Rompun 20 in a 1:2 ratio and administered via intraperitoneal injection at a dosage of 0.1 mL per 100 g of body weight. After anesthesia was achieved, 200 μL of the respective sample was directly injected into the subcutaneous tumor site. The animals were then exposed to AMF (750–1150 kHz) for 300s. An IR camera was used to monitor the therapeutic temperature during treatment. To assess the retention and therapeutic temperature of the materials, IR thermal imaging and tumor growth were monitored on days 0, 5, 7, 10, 15, and 21. Body weight was recorded throughout the experiment to monitor systemic health. Burning areas were calculated based on IR images using Image J software.

At the end of the experiment, animals were euthanized using CO_2 inhalation, and tumors along with major organs (heart, liver, spleen, lungs, and kidneys) were harvested and fixed in formalin. Histological evaluations, including hematoxylin and eosin (H&E) and Masson's trichrome staining, were performed by Toson Technology Co., Ltd. (Taiwan). The stained tissues were scanned and analyzed for pathological assessment. To evaluate systemic toxicity and organ function, blood biochemical tests were conducted at weeks 1, 2, and 3 post-treatment. Renal function was assessed by measuring blood urea nitrogen (BUN) and creatinine (CRE) levels, while hepatic function was evaluated based on aspartate aminotransferase (AST) and alanine aminotransferase (ALT) levels.

5.12 | Retention Assay under Shear Flow

To evaluate the role of particle surface morphology in retention under shear stress, a flushing assay was conducted using HepG2 cells as a model substrate. Two types of pollen-derived microgels were tested: spiky-structured sunflower PM and smooth-surfaced camellia PM, representing distinct geometries.

HepG2 cells were seeded at a density of 1×10^5 cells per well in standard 6-well plates and allowed to adhere for 48 h under standard culture conditions (37°C, 5% CO_2). After incubation, the culture medium was carefully removed and washed by PBS twice, adding a minimal volume (0.5 mL) to maintain surface moisture without disturbing the cell monolayer. Each type of PM was suspended in fresh culture medium at a concentration of 10 mg/mL and homogenized by vortexing for 30 s. The particle-containing medium was then continuously delivered onto the cell surface using a peristaltic pump at a constant flow rate of 100 μL/min, without prior static incubation. This allowed real-time assessment of particle adhesion from the moment of contact. Time-lapse images were captured at 1, 20, 40, and 60 min using an inverted microscope to monitor particle retention under flow. Retention efficiency was quantified by measuring the total number of particles remaining on the surface at each time point using ImageJ. This setup allowed direct comparison between the adhesion behavior of spiky sunflower PM and smooth camellia PM under dynamic shear conditions.

5.13 | Statistical Analysis

All experimental data were analyzed using Origin software (OriginLab Corporation, USA). Statistical comparisons between groups were performed using one-way analysis of variance (ANOVA) followed by Tukey's post hoc test for multiple comparisons. All experiments were conducted in a completely randomized design. Data are presented as mean ± standard deviation (SD). Statistical significance was defined as $*p < 0.05$, $**p < 0.01$, and $***p < 0.001$. Differences with $p > 0.05$ were considered not statistically significant.

Acknowledgements

The authors would like to thank Dr. Hyunhyuk Tae for his valuable guidance on the preparation and use of cationic liposomes. This work was supported by Nanyang Technological University, Singapore, and funded by the Ministry of Education (MOE), Singapore, under the Academic Research Fund Tier 3 (Award No. MOET32022-0002), and by the National Research Foundation, Prime Minister's Office, Singapore, through its Campus for Research Excellence and Technological Enterprise (CREATE) program via the Cellular Agriculture (CellAg) Program (Grant No. 370184512). The authors thank colleagues from the Translational Science for Sustainable Materials (TSSM) and the Centre for Cross Economy (CCE), NTU, for their valuable insights. Financial support from the National Science and Technology Council of Taiwan (NSTC 112-2221-E-027-038-MY3) is gratefully acknowledged. Technical assistance with SQUID measurements from the Instrumentation Center, National Taiwan University, and from the Precision Analysis and Material Research Center, National Taipei University of Technology, is also appreciated.

Funding

This work was supported by Nanyang Technological University, Singapore, and funded by the Ministry of Education (MOE), Singapore, under the Academic Research Fund Tier 3 (Award No. MOET32022-0002), and by the National Research Foundation, Prime Minister's Office, Singapore, through its Campus for Research Excellence and Technological Enterprise (CREATE) program via the Cellular Agriculture (CellAg) Program (Grant No. 370184512). The National Science and Technology Council of Taiwan (NSTC 112-2221-E-027-038-MY3).

Conflicts of Interest

N.-J.C. is the inventor or co-inventor on Singapore patent applications filed as Technology Disclosures (TD) related to pollen-based materials innovation technologies. The other authors declare no competing interests.

Data Availability Statement

The data that support the findings of this study are available from the corresponding author upon reasonable request.

References

1. S. Banerjee, C. M. Booth, E. Bruera, et al., "Two Decades of Advances in Clinical Oncology—Lessons Learned and Future Directions," *Nature Reviews Clinical Oncology* 21 (2024): 771–780, https://doi.org/10.1038/s41571-024-00945-4.

2. A. Shakeri-Zadeh and J. W. Bulte, "Imaging-Guided Precision Hyperthermia with Magnetic Nanoparticles," *Nature Reviews Bioengineering* 3 (2025): 245–260, https://doi.org/10.1038/s44222-024-00257-3.

3. L. Beola, N. Iturrioz-Rodríguez, C. Pucci, R. Bertorelli, and G. Ciofani, "Drug-Loaded Lipid Magnetic Nanoparticles for Combined Local Hyperthermia and Chemotherapy Against Glioblastoma Multiforme," *ACS Nano* 17 (2023): 18441–18455, https://doi.org/10.1021/acsnano.3c06085.

4. J. L. Wu, Q. Ji, C. Blackadar, et al., "The Pathways for Nanoparticle Transport Across Tumour Endothelium," *Nature Nanotechnology* 20 (2025): 672–682.

5. T. Lammers, "Nanomedicine Tumor Targeting," *Advanced Materials* 36 (2024): 2312169, https://doi.org/10.1002/adma.202312169.

6. Y. Tang, X. Quan, J. Mei, et al., "A Vascular Heterogeneity-Orienting TACE Strategy Addresses Peripheral Tumor and Avascular Deep Tumor for Complete Hepatocellular Carcinoma Clearance," *Chemical Engineering Journal* 511 (2025): 161996, https://doi.org/10.1016/j.cej.2025.161996.

7. L. N. Nguyen, W. Ngo, Z. P. Lin, et al., "The Mechanisms of Nanoparticle Delivery to Solid Tumours," *Nature Reviews Bioengineering* 2 (2024): 201–213, https://doi.org/10.1038/s44222-024-00154-9.

8. M. Izci, C. Maksoudian, B. B. Manshian, and S. J. Soenen, "The Use of Alternative Strategies for Enhanced Nanoparticle Delivery to Solid Tumors," *Chemical Reviews* 121 (2021): 1746–1803, https://doi.org/10.1021/acs.chemrev.0c00779.

9. Y.-H. Cheng, C. He, J. E. Riviere, N. A. Monteiro-Riviere, and Z. Lin, "Meta-Analysis of Nanoparticle Delivery to Tumors Using a Physiologically Based Pharmacokinetic Modeling and Simulation Approach," *ACS Nano* 14 (2020): 3075–3095, https://doi.org/10.1021/acsnano.9b08142.

10. L. N. Nguyen, Z. P. Lin, S. Sindhwani, et al., "The Exit of Nanoparticles From Solid Tumours," *Nature Materials* 22 (2023): 1261–1272, https://doi.org/10.1038/s41563-023-01630-0.

11. J. Nowak-Jary and B. Machnicka, "In Vivo Biodistribution and Clearance of Magnetic Iron Oxide Nanoparticles for Medical Applications," *International Journal of Nanomedicine* 18 (2023): 4067–4100, https://doi.org/10.2147/IJN.S415063.

12. T. Haber, Y. R. Cornejo, S. Aramburo, et al., "Specific Targeting of Ovarian Tumor-Associated Macrophages by Large, Anionic Nanoparticles," *Proceedings of the National Academy of Sciences* 117 (2020): 19737–19745, https://doi.org/10.1073/pnas.1917424117.

13. H. Cabral, J. Li, K. Miyata, and K. Kataoka, "Controlling the Biodistribution and Clearance of Nanomedicines," *Nature Reviews Bioengineering* 2 (2024): 214–232, https://doi.org/10.1038/s44222-023-00138-1.

14. C. Caro, C. Guzzi, I. Moral-Sánchez, J. D. Urbano-Gámez, A. M. Beltrán, and M. L. García-Martín, "Smart Design of ZnFe and ZnFe@Fe Nanoparticles for MRI-Tracked Magnetic Hyperthermia Therapy: Challenging Classical Theories of Nanoparticles Growth and Nanomagnetism," *Advanced Healthcare Materials* 13 (2024): 2304044, https://doi.org/10.1002/adhm.202304044.

15. X. Yuan, X. Liu, H. Li, et al., "pH-Triggered Transformable Peptide Nanocarriers Extend Drug Retention for Breast Cancer Combination Therapy," *Advanced Healthcare Materials* 13 (2024): 2400031, https://doi.org/10.1002/adhm.202400031.

16. F. Gao, L. Zhu, L. Jiang, et al., "Enhanced Penetration and Retention of CuS-Based Nanosystem Through NIR Light and In Situ Enzyme Response for Improved Tumor Therapy," *Advanced Functional Materials* 34 (2024): 2312182, https://doi.org/10.1002/adfm.202312182.

17. W. Zhen, R. R. Weichselbaum, and W. Lin, "Nanoparticle-Mediated Radiotherapy Remodels the Tumor Microenvironment to Enhance Antitumor Efficacy," *Advanced Materials* 35 (2023): 2206370, https://doi.org/10.1002/adma.202206370.

18. M. Xu, Y. Qi, G. Liu, Y. Song, X. Jiang, and B. Du, "Size-Dependent In Vivo Transport of Nanoparticles: Implications for Delivery, Targeting, and Clearance," *ACS Nano* 17 (2023): 20825–20849, https://doi.org/10.1021/acsnano.3c05853.

19. P. Dosta, M. Z. Dion, M. Prado, et al., "Matrix Metalloproteinase- and pH-Sensitive Nanoparticle System Enhances Drug Retention and Penetration in Glioblastoma," *ACS Nano* 18 (2024): 14145–14160, https://doi.org/10.1021/acsnano.3c03409.

20. A. Dasgupta, A. M. Sofias, F. Kiessling, and T. Lammers, "Nanoparticle Delivery to Tumours: From EPR and ATR Mechanisms to Clinical Impact," *Nature Reviews Bioengineering* 2 (2024): 714–716, https://doi.org/10.1038/s44222-024-00203-3.

21. H. Gavilán, G. M. Rizzo, N. Silvestri, B. T. Mai, and T. Pellegrino, "Scale-Up Approach for the Preparation of Magnetic Ferrite Nanocubes and Other Shapes with Benchmark Performance for Magnetic Hyperthermia Applications," *Nature Protocols* 18 (2023): 783–809, https://doi.org/10.1038/s41596-022-00779-3.

22. Y. Cai, X. Kang, L. Zhou, et al., "Multifunctional Superparamagnetic Copper Iron Oxide Nanoparticles for Synergistic Cancer Therapy via Magnetic Hyperthermia, Oxidative Stress and Immune Reprogramming," *Advanced Functional Materials* 35 (2025): 2425286, https://doi.org/10.1002/adfm.202425286.

23. S. Lukácsi, G. Munkácsy, and B. Győrffy, "Harnessing Hyperthermia: Molecular, Cellular, and Immunological Insights for Enhanced Anticancer Therapies," *Integrative Cancer Therapies* 23 (2024): 15347354241242094, https://doi.org/10.1177/15347354241242094.

24. E. C. Lerner, R. M. Edwards, D. S. Wilkinson, and P. E. Fecci, "Laser Ablation: Heating up the Anti-Tumor Response in the Intracranial Compartment," *Advanced Drug Delivery Reviews* 185 (2022): 114311, https://doi.org/10.1016/j.addr.2022.114311.

25. M. S. Ibrahim, A. R. Ferhan, C. Zhou, et al., "Allergen to Asset: Pollen-Based Drug Delivery Systems," *Advanced Drug Delivery Reviews* 224 (2025): 115643, https://doi.org/10.1016/j.addr.2025.115643.

26. Y. Kittel, A. J. Kuehne, and L. De Laporte, "Translating Therapeutic Microgels Into Clinical Applications," *Advanced Healthcare Materials* 11 (2022): 2101989, https://doi.org/10.1002/adhm.202101989.

27. M. Liu, Y. Cao, Z. Li, E. Wang, R. J. Ram, and B. Marelli, "Precise and High-Throughput Delivery of Micronutrients in Plants Enabled by Pollen-Inspired Spiny and Biodegradable Microcapsules," *Advanced Materials* 36 (2024): 2401192, https://doi.org/10.1002/adma.202401192.

28. W. Hu, Z. Zhou, F. Zou, et al., "Harnessing Natural Pollen as Sustained-Release, Mucoadhesive, and Biosafe Drug Microcapsules for Intravesical Instillation in Bladder Cancer Treatment," *Small* 21 (2025): 2406351, https://doi.org/10.1002/smll.202406351.

29. D. Zhao, X. Li, Q. Guo, et al., "Recent Advances in Spiky Pollen-Inspired Functional Microparticles," *Applied Materials Today* 35 (2023): 101988, https://doi.org/10.1016/j.apmt.2023.101988.

30. J. Deng, Z. Zhao, X. Y. Yeo, et al., "Plant-Based Shape Memory Cryogel for Hemorrhage Control," *Advanced Materials* 36 (2024): 2311684, https://doi.org/10.1002/adma.202311684.

31. T.-F. Fan, S. Park, Q. Shi, et al., "Transformation of Hard Pollen Into Soft Matter," *Nature Communications* 11 (2020): 1449, https://doi.org/10.1038/s41467-020-15294-w.

32. H. Tae, S. Park, L. Y. Tan, et al., "Elucidating Structural Configuration of Lipid Assemblies for mRNA Delivery Systems," *ACS Nano* 18 (2024): 11284–11299, https://doi.org/10.1021/acsnano.4c00587.

33. A. F. Edlund, K. Olsen, C. Mendoza, et al., "Pollen Wall Degradation in the Brassicaceae Permits Cell Emergence After Pollination," *American Journal of Botany* 104 (2017): 1266–1273, https://doi.org/10.3732/ajb.1700201.

34. J. Li, J. Deng, C. Zhou, et al., "Biomimetic Superhydrophobic Surfaces by Nanoarchitectonics with Natural Sunflower Pollen," *Small* 21 (2025): 2409136, https://doi.org/10.1002/smll.202409136.

35. C. Zhou, J. Deng, T. J. Hao, et al., "Multifunctional Material Building Blocks From Plant Pollen," *Annual Review of Chemical and Biomolecular Engineering* 15 (2024): 1–24, https://doi.org/10.1146/annurev-chembioeng-101121-085959.

36. C. Chen, H. Yuan, X. Wang, Y. Lin, Y. He, and F. Wang, "Recyclable and High-Efficiency Methane Hydrate Formation Promoter Based on SDS-Coated Superparamagnetic Nano-Fe_3O_4," *Chemical Engineering Journal* 437 (2022): 135365, https://doi.org/10.1016/j.cej.2022.135365.

37. W. M. Daoush, "Co-Precipitation and Magnetic Properties of Magnetite Nanoparticles for Potential Biomedical Applications," *Journal of Nanomedicine Research* 5 (2017): 00118.

38. K. S. Muthiah, S. R. Natarajan, S. Jayaraman, U. Dhawan, Y.-C. Lin, and R.-J. Chung, "Photo-Responsive g-C_3N_4/Copper Molybdate Nanocomposites Enable Laser-Driven Multi-Modal Imaging, Photothermal and Chemodynamic Therapy for Hepatocellular Carcinoma Treatment," *Chemical Engineering Journal* 507 (2025): 160751, https://doi.org/10.1016/j.cej.2025.160751.

39. Y. Ueda, S. Kiyonaka, L. M. Selfors, et al., "Intratumour Oxidative Hotspots Provide a Niche for Cancer Cell Dissemination," *Nature Cell Biology* 27 (2025): 530–543.

40. L. Yu, Y. Tian, A. Gao, Z. Shi, Y. Liu, and C. Li, "Bi-Module Sensing Device to In Situ Quantitatively Detect Hydrogen Peroxide Released from Migrating Tumor Cells," *PLoS One* 10 (2015): 0127610.

41. A. A. Dobritsa, A. Geanconteri, J. Shrestha, et al., "A Large-Scale Genetic Screen in Arabidopsis to Identify Genes Involved in Pollen Exine Production," *Plant Physiology* 157 (2011): 947–970, https://doi.org/10.1104/pp.111.179523.

42. L. Albano, A. Bento, V. G. Correia, and C. S. Pereira, "The Chemistry of Sporopollenin Ektexine and Endexine Layers Isolated From Sunflower Pollen Through an Ionic Liquid-Mediated Process," *ACS Omega* 10 (2024): 411–421, https://doi.org/10.1021/acsomega.4c06524.

43. J. M. Ageitos, S. Robla, L. Valverde-Fraga, M. Garcia-Fuentes, and N. Csaba, "Purification of Hollow Sporopollenin Microcapsules From Sunflower and Chamomile Pollen Grains," *Polymers* 13 (2021): 2094, https://doi.org/10.3390/polym13132094.

44. Y. C. Lin, C. Y. Lee, J. R. Jones, et al., "Sustained Antibiotic Release From Biodegradable Gelatin–Silica Hybrid for Orthopedic Infections," *Advanced Functional Materials* 34 (2024): 2409491, https://doi.org/10.1002/adfm.202409491.

45. Z. Gu, Y. Dong, S. Xu, L. Wang, and Z. Liu, "Molecularly Imprinted Polymer-Based Smart Prodrug Delivery System for Specific Targeting, Prolonged Retention, and Tumor Microenvironment-Triggered Release," *Angewandte Chemie* 133 (2021): 2695–2699, https://doi.org/10.1002/ange.202012956.

46. A. Smirnova, N. Matveyeva, and I. Yermakov, "Reactive Oxygen Species are Involved in Regulation of Pollen Wall Cytomechanics," *Plant Biology* 16 (2014): 252–257, https://doi.org/10.1111/plb.12004.

47. Q. Lu, R. Chen, F. Zeng, et al., "Inhalation of Bioorthogonal Gene-Editable Spiky-Pollen Reprograms Tumor-Associated Macrophages for

Lung Cancer Immunotherapy," *Advanced Functional Materials* 34 (2024): 2408767, https://doi.org/10.1002/adfm.202408767.

48. S. Gao, T. Yan, L. Ji, et al., "Pathologically Responsive Au@Ag Nanocomposite Spray-Coated Hydrogel Dressing for Accelerated Healing of Infected Wounds," *ACS Applied Materials & Interfaces* 17 (2025): 46693–46704, https://doi.org/10.1021/acsami.5c10248.

49. L. Liu, W. Wang, L. Huang, et al., "Injectable Pathological Microenvironment-Responsive Anti-Inflammatory Hydrogels for Ameliorating Intervertebral Disc Degeneration," *Biomaterials* 306 (2024): 122509, https://doi.org/10.1016/j.biomaterials.2024.122509.

50. S. He, Z. Li, L. Wang, et al., "A Nanoenzyme-Modified Hydrogel Targets Macrophage Reprogramming-Angiogenesis Crosstalk to Boost Diabetic Wound Repair," *Bioactive materials* 35 (2024): 17–30, https://doi.org/10.1016/j.bioactmat.2024.01.005.

51. H. Tae, S. Park, Y. Choe, C. Yang, and N.-J. Cho, "Exploring the Interfacial Dynamics of Unilamellar and Multilamellar Cationic Liposomes on SiO_2 and Their Interactions with Membrane-Active Peptide," *Langmuir* 40 (2024): 24761–24770, https://doi.org/10.1021/acs.langmuir.4c02273.

52. T. Saragi, B. Depi, S. Butarbutar, and B. Permana, "The Impact of Synthesis Temperature on Magnetite Nanoparticles Size Synthesized by Co-Precipitation Method," *Journal of Physics: Conference Series* 1031 (2018): 012190.

53. W. R. Smythe, "*Static and Dynamic Electricity*", (Taylor &Francis, 1988).

54. J. C. Maxwell, "A Treatise on Electricity and Magnetism, Clarendon," *Oxford* 314 (1881): 1873.

55. D. J. Griffiths, *Introduction to Electrodynamics* (Cambridge University Press, 2023), https://doi.org/10.1017/9781009397735.

Supporting Information

Additional supporting information can be found online in the Supporting Information section.

Supporting File: adfm73785-sup-0001-SuppMat.docx.